Search for Proton Decay via $p \to \nu K^+$ using 260 kiloton·year data of Super-Kamiokande

K. Abe,[1,26] Y. Hayato,[1,26] K. Iyogi,[1] J. Kameda,[1,26] M. Miura,[1,26] S. Moriyama,[1,26] M. Nakahata,[1,26] S. Nakayama,[1,26]
R. A. Wendell,[1,26] H. Sekiya,[1,26] M. Shiozawa,[1,26] Y. Suzuki,[1,26] A. Takeda,[1,26] Y. Takenaga,[1] K. Ueno,[1] T. Yokozawa,[1]
H. Kaji,[2] T. Kajita,[2,26] K. Kaneyuki,[2,26,*] K. P. Lee,[2] K. Okumura,[2] T. McLachlan,[2] L. Labarga,[3] E. Kearns,[4,26]
J. L. Raaf,[4] J. L. Stone,[4,26] L. R. Sulak,[4] M. Goldhaber,[5,*] K. Bays,[6] G. Carminati,[6] W. R. Kropp,[6] S. Mine,[6]
A. Renshaw,[6] M. B. Smy,[6,26] H. W. Sobel,[6,26] K. S. Ganezer,[7] J. Hill,[7] W. E. Keig,[7] J. S. Jang,[8] J. Y. Kim,[8] I. T. Lim,[8]
J. B. Albert,[9] K. Scholberg,[9,26] C. W. Walter,[9,26] T. Wongjirad,[9] T. Ishizuka,[10] S. Tasaka,[11] J. G. Learned,[12]
S. Matsuno,[12] S. N. Smith,[12] T. Hasegawa,[13] T. Ishida,[13] T. Ishii,[13] T. Kobayashi,[13] T. Nakadaira,[13] K. Nakamura,[13,26]
K. Nishikawa,[13] Y. Oyama,[13] K. Sakashita,[13] T. Sekiguchi,[13] T. Tsukamoto,[13] A. T. Suzuki,[14] Y. Takeuchi,[14] K. Ieki,[15]
M. Ikeda,[15] H. Kubo,[15] A. Minamino,[15] A. Murakami,[15] T. Nakaya,[15,26] Y. Fukuda,[16] K. Choi,[17] Y. Itow,[17]
G. Mitsuka,[17] M. Miyake,[17] P. Mijakowski,[29] J. Hignight,[18] J. Imber,[18] C. K. Jung,[18] I. Taylor,[18] C. Yanagisawa,[18]
H. Ishino,[19] A. Kibayashi,[19] Y. Koshio,[19] T. Mori,[19] M. Sakuda,[19] J. Takeuchi,[19] Y. Kuno,[20] S. B. Kim,[21] H. Okazawa,[22]
Y. Choi,[23] K. Nishijima,[24] M. Koshiba,[25] Y. Totsuka,[25,*] M. Yokoyama,[25,26] K. Martens,[26] Ll. Marti,[26] Y. Obayashi,[26]
M. R. Vagins,[26,6] S. Chen,[27] H. Sui,[27] Z. Yang,[27] H. Zhang,[27] K. Connolly,[28] M. Dziomba,[28] and R. J. Wilkes[28]

(The Super-Kamiokande Collaboration)

[1]*Kamioka Observatory, Institute for Cosmic Ray Research, University of Tokyo, Kamioka, Gifu 506-1205, Japan*
[2]*Research Center for Cosmic Neutrinos, Institute for Cosmic Ray Research, University of Tokyo, Kashiwa, Chiba 277-8582, Japan*
[3]*Department of Theoretical Physics, University Autonoma Madrid, 28049 Madrid, Spain*
[4]*Department of Physics, Boston University, Boston, MA 02215, USA*
[5]*Physics Department, Brookhaven National Laboratory, Upton, NY 11973, USA*
[6]*Department of Physics and Astronomy, University of California, Irvine, Irvine, CA 92697-4575, USA*
[7]*Department of Physics, California State University, Dominguez Hills, Carson, CA 90747, USA*
[8]*Department of Physics, Chonnam National University, Kwangju 500-757, Korea*
[9]*Department of Physics, Duke University, Durham NC 27708, USA*
[10]*Junior College, Fukuoka Institute of Technology, Fukuoka, Fukuoka 811-0295, Japan*
[11]*Department of Physics, Gifu University, Gifu, Gifu 501-1193, Japan*
[12]*Department of Physics and Astronomy, University of Hawaii, Honolulu, HI 96822, USA*
[13]*High Energy Accelerator Research Organization (KEK), Tsukuba, Ibaraki 305-0801, Japan*
[14]*Department of Physics, Kobe University, Kobe, Hyogo 657-8501, Japan*
[15]*Department of Physics, Kyoto University, Kyoto, Kyoto 606-8502, Japan*
[16]*Department of Physics, Miyagi University of Education, Sendai, Miyagi 980-0845, Japan*
[17]*Solar Terrestrial Environment Laboratory, Nagoya University, Nagoya, Aichi 464-8602, Japan*
[18]*Department of Physics and Astronomy, State University of New York at Stony Brook, NY 11794-3800, USA*
[19]*Department of Physics, Okayama University, Okayama, Okayama 700-8530, Japan*
[20]*Department of Physics, Osaka University, Toyonaka, Osaka 560-0043, Japan*
[21]*Department of Physics, Seoul National University, Seoul 151-742, Korea*
[22]*Department of Informatics in Social Welfare, Shizuoka University of Welfare, Yaizu, Shizuoka, 425-8611, Japan*
[23]*Department of Physics, Sungkyunkwan University, Suwon 440-746, Korea*
[24]*Department of Physics, Tokai University, Hiratsuka, Kanagawa 259-1292, Japan*
[25]*The University of Tokyo, Bunkyo, Tokyo 113-0033, Japan*
[26]*Kavli Institute for the Physics and Mathematics of the Universe (WPI), Todai Institutes for Advanced Study, University of Tokyo, Kashiwa, Chiba 277-8582, Japan*
[27]*Department of Engineering Physics, Tsinghua University, Beijing, 100084, China*
[28]*Department of Physics, University of Washington, Seattle, WA 98195-1560, USA*
[29]*National Centre For Nuclear Research, 00-681 Warsaw, Poland*
(Dated: August 7, 2014)

We have searched for proton decay via $p \to \nu K^+$ using Super-Kamiokande data from April 1996 to February 2013, 260 kiloton·year exposure in total. No evidence for this proton decay mode is found. A lower limit of the proton lifetime is set to $\tau/B(p \to \nu K^+) > 5.9 \times 10^{33}$ years at 90% confidence level.

I. INTRODUCTION

---

*Deceased.

The standard model of particle physics, based on $SU(3)$ for the strong interaction and the unification of $SU(2) \times U(1)$ for the electroweak interaction, has been successful in accounting

for many experimental results. However, the standard model offers no guidance on the unification of the strong and electroweak forces, and has many other open questions. Various attempts have been made to resolve the shortcomings by unifying the strong and electroweak interactions in a single larger gauge group, i.e. a Grand Unified Theory (GUT) [1]. GUTs are motivated by the apparent convergence of the running couplings of the strong, weak, and electromagnetic forces at a high energy scale ($10^{15} - 10^{16}$ GeV). Energy scales this large are out of the reach of accelerators but may be probed by virtual processes such as those that govern particle decay. A general feature of GUTs is the instability of nucleons by baryon number violating decay. Nucleon decay experiments are direct experimental tests of the general idea of grand unification.

In GUTs, nucleon decay can proceed via exchange of a massive gauge boson between two quarks. The favored gauge-mediated decay mode in many GUTs is $p \rightarrow e^+\pi^0$. In the minimal SU(5) GUT, the predicted proton lifetime to $e^+\pi^0$ is $10^{31\pm1}$ years, which has been ruled out by experimental results from IMB [2], Kamiokande [3], and Super-Kamiokande [4]. GUT models incorporating supersymmetry [6] (SUSY-GUTs) raise the GUT scale [7], suppressing the decay rate of $p \rightarrow e^+\pi^0$, thereby allowing compatibility with the experimental limit. However, SUSY-GUTs introduce dimension five operators that enable the mode $p \rightarrow \overline{\nu}K^+$ to have a high branching fraction and short partial lifetime [8]. In the SUSY SU(5) GUT with minimal assumptions and TeV scale SUSY particles, the partial proton lifetime to $\overline{\nu}K^+$ is less than 10^{31} years [9], which has also been excluded by previously published experimental constraints [2, 3, 5]. Non-minimal SUSY SU(5) GUTs [11] or SUSY GUTs based on SO(10) [12] have been constructed that evade this limit, yet still predict partial lifetimes in the range 10^{32} to 10^{35} years, with some particular models that require the lifetime be less than a few times 10^{34} years. The low ends of the lifetime predictions by these models are probed by this experimental search.

In this paper, our search is for the two-body decay of proton to a K^+ and a neutrino. In most models, $(B - L)$ is conserved and the final state contains an anti-neutrino; however we do not detect the neutrino and cannot distinguish $p \rightarrow \nu K^+$ from $p \rightarrow \overline{\nu}K^+$, nor can we determine the flavor (e, μ, or τ) of the neutrino. In fact, our search can be applied to any nearly massless neutral final-state particle such as a gravitino or axino.

The Super-Kamiokande collaboration published a search for $p \rightarrow \nu K^+$ with 91.7 kton·years exposure of the first phase of the experiment, and set a partial lifetime limit $\tau(p \rightarrow \nu K^+) > 2.3 \times 10^{33}$ years [10]. In this paper, we refine the analysis and update the search with 2.8 times greater detector exposure including later phases of the experiment.

II. SUPER-KAMIOKANDE DETECTOR

Super-Kamiokande [13] is a large water Cherenkov detector. It is an upright cylinder in shape, 39 m in diameter and 40 m in height, and it contains 50 kton of pure water. It lies about 1,000 m underneath the top of Mt. Ikenoyama (2,700 m

	Live days	kton·yr	Coverage	Note
SK-I	1489.2	91.7	40%	
SK-II	798.6	49.2	19%	Half PMT density
SK-III	518.1	31.9	40%	
SK-IV	1417.4	87.3	40%	New readout electronics

TABLE I: Summary of data sets that are used in this paper.

water equivalent underground) to reduce cosmic ray background. The detector is optically separated into two regions: inner detector (ID) and outer detector (OD). Cherenkov light in the ID is detected by 20-inch PMTs [14] facing inward, evenly covering the cylindrical inner surface. Cherenkov light from penetrating particles, usually cosmic ray muons or exiting muons, is detected by 8-inch PMTs facing outward. The fiducial volume is defined as a cylindrical volume with surfaces 2 meters inwards from the ID PMT plane. The fiducial mass is 22.5 ktons, corresponding to 7.5×10^{33} protons.

Super-Kamiokande started observation in April 1996 with 11,146 PMTs which covered 40% of the ID surface. The observation was continued until July 2001, with 1489.2 live days, or equivalently, 91.7 kton·years. This period is called Super-Kamiokande-I (SK-I). After an accident in 2001, about half of the ID PMTs were lost and the detector was reconstructed with 5,182 ID PMTs uniformly distributed over the cylindrical surface decreasing photo coverage to 19%. The PMTs were thereafter enclosed in acrylic and FRP cases. The period from December 2002 until October 2005, corresponding to 798.6 live days (49.2 kton·years), is called SK-II. After production and installation of replacement 20-inch PMTs, the photo coverage was recovered to 40% in 2006. The period between July 2006 and September 2008, corresponding to 518.1 live days (31.9 kton·years), is defined as SK-III. In the summer of 2008, we upgraded our electronics with improved performance including a data acquisition that records all PMT hit information without dead time [15]. This has been the configuration of the detector since September 2008; it is called SK-IV. In this paper, we use data until February 2013, corresponding to 1417.4 live days (87.3 kton·years). Table I summarizes the data sets used for the proton decay search in this paper.

The trigger to record an event is based on the coincidence of the number of hit PMTs exceeding a threshold. For SK I-III, the trigger was implemented in hardware using a signal proportional to the number of hit PMTs produced by each front-end electronics module. For SK-IV, the trigger is implemented in software. The trigger threshold is less than 10 MeV for all SK periods, and the trigger efficiency for this proton decay mode is 100%[1].

The charge and timing of the PMTs are calibrated using various calibration sources [16]. The timing resolution of the 20-

---

[1] For the case of prompt gamma tag (Method 1), with gamma energy typically 6 MeV, the muon from K^+ decay can provide the event trigger.

inch PMT is about 2.1 nsec at the single photo-electron level. The PMT response, water quality, and reflections from the detector wall are tuned in the SK detector simulation program using injected light as well as various control data samples such as cosmic ray muons.

III. SIMULATION

To determine selection criteria for the proton decay search, and to estimate efficiencies and background rates, we use proton decay and atmospheric neutrino Monte Carlo (MC) simulations. Because the configuration of the detector is different in SK-I through IV, we generated MC samples for each period. Proton decay MC samples with 50,000 events are generated in an oversized volume which is 1 meter outside the fiducial volume boundary, and therefore 1 meter from the detector wall. This allows us to include event migration near the fiducial boundary in our estimates. The selection efficiency is defined as the number of events fulfilling all requirements divided by number of generated events in the fiducial volume. The MC equivalent of 500 years of atmospheric neutrino exposure are generated for each period. These atmospheric neutrino MC samples are used for our studies of neutrino oscillations [17]. Because the background rates for the proton decay studied in this paper are small (less than one event for the entire exposure for two of the analysis techniques), these large MC background samples provide fewer than 40 atmospheric neutrino events that survive the proton decay selection criteria.

A. Proton Decay

A water molecule contains two free protons and eight protons bound in the oxygen nucleus. In the decay of a free proton, the ν and the K^+ are emitted opposite each other with momenta of 339 MeV/c. In the case of proton decay in oxygen, Fermi momentum, correlation with other nucleons, nuclear binding energy, and kaon-nucleon interactions are taken into account as described below.

We use the Fermi momentum and nuclear binding energy measured by electron-^{12}C scattering [18]. Nuclear binding energy is taken into account by modifying the proton mass. Ten percent of decaying protons are estimated to have wave functions which are correlated with other nucleons within the nucleus [19]. These correlated decays cause the total invariant mass of the decay products to be smaller than the proton mass because of the momentum carried by the correlated nucleons. Figure 1 shows the invariant mass of the products of the decaying proton, K^+ and ν and the resulting kaon momenta after the simulation of the proton decay for both bound and free protons. Correlated decays produce the broad spectrum below about 850 MeV/c^2. In our experiment, the kaon momentum is unobserved because the kaon is always produced below the Cherenkov threshold of 749 MeV/c in water. The majority of K^+ (89%) are stopped in water and decay at rest. We search

for K^+ decay at rest into $\mu^+\nu_\mu$ (64% branching fraction) and $\pi^+\pi^0$ (21% branching fraction).
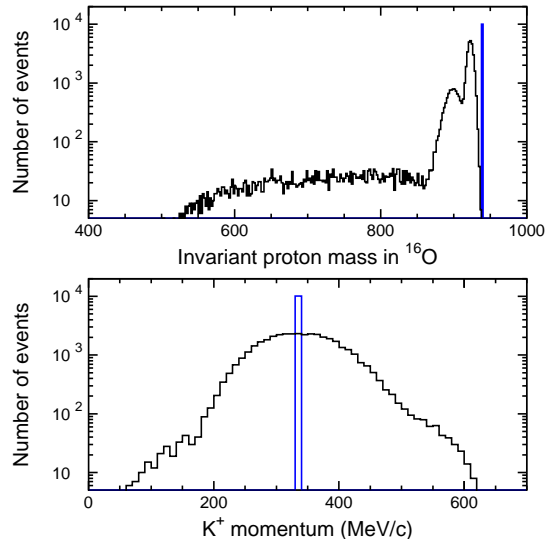

FIG. 1: (color online) The upper figure shows the decaying proton mass distribution in ^{16}O and the lower figure shows the K^+ momentum distribution from the simulation of $p \rightarrow \nu K^+$. In the upper figure, the single-bin histogram shows the free proton case and the broad histogram shows the bound proton case. The rightmost peak in the bound proton case corresponds to the p-state, located slightly lower than the proton mass by 15.5 MeV of binding energy; the second rightmost peak is the s-state (39 MeV in binding energy). The correlated nucleon decay makes the longer tail in the lower mass region. In the lower figure, the single-bin histogram shows the free proton case (339 MeV/c) and the broad histogram shows the bound proton case which is smeared by Fermi motion.

The position of the decaying proton in ^{16}O is calculated according to the Woods-Saxon nuclear density model [20]. The kaon nucleon interactions which are considered include elastic scattering and inelastic scattering via charge exchange. The type of interaction is determined using the calculated mean free path [21]. For kaons, whose momenta are described by Fig. 1, the probability of charge exchange for K^+ in $p \rightarrow \nu K^+$ is 0.14%.

If a nucleon decays in the oxygen nucleus, the remaining nucleus can be left in an excited state from which it promptly de-excites by the emission of gamma rays. The prompt gamma emission processes are simulated based on reference [23]. The dominant gamma ray is 6.3 MeV from the $p_{3/2}$ state with 41% branching fraction. The probabilities of γ emission in this simulation are summarized in Table II. Other states emitting low energy gamma rays are averaged and assigned 3.5 MeV γ emission. Nuclear decay into states that emit protons or neutrons and nuclear decay into the ground state are taken to have no γ ray emission.

State	Energy of γ	Probability
$p_{3/2}$	6.3 MeV	41%
$p_{3/2}$	9.9 MeV	3%
$s_{1/2}$	7.03 MeV	2%
$s_{1/2}$	7.01 MeV	2%
others	3.5 MeV	16%
Other than γ emission		
p/n emission	-	11%
ground state	-	25%

TABLE II: Summary of probabilities of nuclear γ ray emissions at the de-excitation of the remaining nucleus.

B. Atmospheric Neutrinos

The SK standard atmospheric neutrino MC used in the previous neutrino oscillation analyses [17] and proton decay searches [4, 10, 24, 25] is used in this analysis. It is based on the Honda atmospheric neutrino flux [26] and NEUT [21] neutrino-nucleus interaction model. Some neutrino interactions which produce K mesons via resonances could be potential background sources for $p \to \nu K^+$ search. Cross sections of the single meson production via resonances are calculated based on Rein and Sehgal's theory [22]. In NEUT, the neutrino reactions:

$$\nu\, n \to l^- \, \Lambda\, K^+$$
$$\nu\, n \to \nu\, \Lambda\, K^0$$
$$\nu\, p \to \nu\, \Lambda\, K^+$$
$$\overline{\nu}\, p \to l^+ \, \Lambda\, K^0$$
$$\overline{\nu}\, n \to \overline{\nu}\, \Lambda\, K^0$$
$$\overline{\nu}\, p \to \overline{\nu}\, \Lambda\, K^+$$

are taken into account assuming the same cross section both for ν_e and ν_μ. The differential cross sections are shown in Fig. 2.

We simulate propagation of the produced particles and Cherenkov light in water by custom code based on GEANT3 [27]. The propagation of charged pions in water is simulated by custom code based on Ref. [28] for less than 500 MeV/c and by GCALOR [29] for more than 500 MeV/c.

The equivalent of 500 years of SK atmospheric neutrino data is simulated for each SK run period. The generated atmospheric neutrino samples are weighted to include the effect of ν_μ disappearance due to ν_μ-ν_τ oscillation assuming $\Delta m^2 = 2.5 \times 10^{-3}$ eV^2 and $\sin^2 2\theta = 1.0$, ignoring the appearance of ν_e or ν_τ as a possible background. The final background event rates for each period are normalized by the observed total sub-GeV event rate.
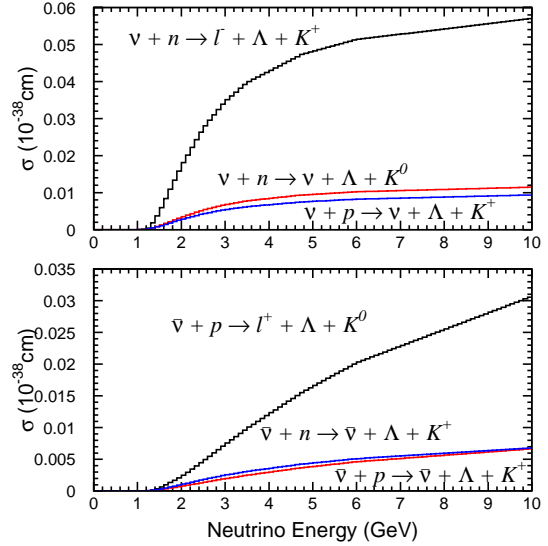

FIG. 2: (color online) Cross sections of the single K-meson productions via resonances calculated by NEUT. Upper plots show neutrino interactions and lower show anti-neutrino interactions.

IV. DATA SET, REDUCTION AND RECONSTRUCTION

The vast majority of the triggered events are cosmic ray muons and low energy backgrounds from the radioactivity of materials around the detector wall. Several stages of data reduction were applied to the events before proceeding to further detailed event reconstruction processes. Details of the data reduction and reconstruction can be found in [17].

The fully contained (FC) data sample in the fiducial volume (FV) is defined by the following cuts:

- number of hit PMTs in the largest OD hit cluster is less than 10 for SK-I and 16 for other period.

- total visible energy is greater than 30 MeV in ID

- distance of the reconstructed vertex from the ID PMT surface is greater than 2 meters (corresponding to 22.5 kton of water volume)

The rate of FCFV events is about 8 events per day. The contamination of events other than atmospheric neutrinos is estimated to be less than 1% and composed of cosmic rays that evaded the OD veto and events caused by flashing PMTs.

Reconstruction algorithms are applied to the events remaining after the reduction process to determine the event vertex, the number of Cherenkov rings, the particle type of each ring, the momentum assigned to each ring, and number of Michel electrons. As a first step, the event vertex is defined as the point at which the timing distribution, after subtraction of the calculated time of flight of the photon from the vertex (TOF subtraction), has the sharpest peak. The dominant ring direction is determined from the charge distribution as a function

of angle. Then other ring candidates are searched for using the Hough transform method [30], a technique for extracting a particular shape from an image, assuming all particles are generated in one vertex. Each ring candidate is tested against a likelihood function to remove fake rings before determining the final number of rings. Each ring is classified as e-like (showering type as from $e^{\pm}, \gamma$) or μ-like (non-showering type) based on a likelihood using the ring pattern and Cherenkov opening angle for single ring case, and only ring pattern for multi-ring case.

Michel electrons from the decay of the $\mu^{\pm}$ are tagged by searching for clusters of in-time hits after the primary event. During the SK-I to SK-III periods, there was an impedance mismatch between cables and electronics which caused a signal reflection at 1000 ns after the main event. The time period between 800 ns and 1200 ns from the primary events was excluded for the decay electron search due to this signal reflection. For SK-IV, the new electronics have better impedance matching to avoid signal reflection, and no such exclusion is required. As a result, the tagging efficiency of decay electrons from μ^+ with momentum of 236 MeV/c has been improved from 85% (SK-I, II, and III) to 99% (SK-IV), which improves the selection efficiency for $p \to \nu K^+$.

The momentum for each ring is decided from the charge spatially inside of $70°$ from the ring direction and temporally from -50 nsec to $+250$ nsec around the TOF-subtracted main event peak. The number of photoelectrons from each PMT are corrected by light attenuation in water, PMT acceptance, dark noise, time variation of gain, and track length in the case of μ-like rings. If a Michel electron is within 250 nsec of the parent particle, the time window for momentum determination is shortened and the charge sum is corrected from the nominal $+250$ nsec case. The momentum scale is checked by cosmic ray muons, Michel electrons from the cosmic ray muons which stop in the inner detector, and also the invariant mass distributions of π^0 events produced in atmospheric neutrino interactions. The uncertainty on the momentum scale is less than 3% for the entire period.

An additional precise vertex fitter is applied only for single-ring events. The expected charge for each PMT is calculated using the result of particle identification (e-like or μ-like) and using the momentum estimate. The expected charge is compared with the observed charge by varying the vertex along the particle direction. The estimated vertex resolution for FC single-ring sub-GeV events is about 30 cm.

V. ANALYSIS

If a proton decays by $p \to \nu K^+$, the K^+ itself is not visible in a water Cherenkov detector since its velocity is below Cherenkov threshold. However, the K^+ can be identified by its decay products in the decay modes $K^+ \to \mu^+ \nu$ and $K^+ \to \pi^+ \pi^0$. Being two-body decay processes, the daughter particles have monochromatic momentum in the K^+ rest frame: 236 MeV/c for $\mu^+ \nu_\mu$ and 205 MeV/c for $\pi^+ \pi^0$. There are three established methods for the $p \to \nu K^+$ mode search [5]: (Method 1) since the γ ray is promptly emitted at the time of K^+ production, look for single muon events with a de-excitation γ ray just before the time of the muon; (Method 2) search for an excess of muon events with a momentum of 236 MeV/c in the momentum distribution; and (Method 3) search for $\pi^+ \pi^0$ events with a momentum of 205 MeV/c.

A. Method 1: $K^+ \to \mu^+ \nu$, tag by prompt gamma ray

If this proton decay happens, the Super-K detector should observe a single μ-like ring preceded by PMT hits due to a nuclear deexcitation gamma ray. Figure 3 shows a graphical event display of the PMT hit pattern for an example event, as a Monte Carlo simulation of the proton decay. A prompt gamma ray, a muon, and a Michel electron peak should be observed in order, as seen in another example in Fig. 4, where the time of each particle is labeled as used in the analysis. To search for events tagged by the prompt gamma ray, single-ring μ-like events are selected by requiring the following criteria:

(A-1) a fully contained event with one non-showering (μ-like) ring,

(A-2) there is one Michel decay electron,

(A-3) the reconstructed muon momentum is between 215 and 260 MeV/c,

(A-4) the distance between the vertices of the muon and the Michel electron is less than 200 cm,

(A-5) the TOF-subtracted timing distribution for the muon vertex is required to have a minimum goodness-of-fit (> 0.6),

(A-6) the pattern of the single non-showering ring is more likely to be a muon than a proton: $L_{pr} - L_\mu < 0$, L_{pr}, L_μ are likelihood functions assuming a proton and a muon, which are described later,

(A-7) gamma hits are found: $8 < N_\gamma < 60$ for SK-I, III, and VI, $4 < N_\gamma < 30$ for SK-II

(A-8) the time difference from the gamma tag to the kaon decay is consistent with the kaon lifetime: $t_\mu - t_\gamma < 75$ nsec,

The cut criteria (A-4) and (A-5) are applied to reject events with a high momentum recoil proton (above Cherenkov threshold) accompanied by an invisible muon or charged pion (below the Cherenkov threshold) which produces a Michel electron in its decay chain. Since the particle type of the single non-showering Cherenkov ring is assumed to be that of a muon, the vertex accuracy is worse when the Cherenkov ring is from a recoil proton. The inaccurate vertex determination causes incorrect TOF subtraction of the Cherenkov light. As a result, recoil protons may create a false peak in the time distribution of hit PMTs, which can fake a prompt gamma ray. The event may include Michel electrons from the decay of the invisible muon, but the distance between the misreconstructed vertex and the Michel electron is typically large.
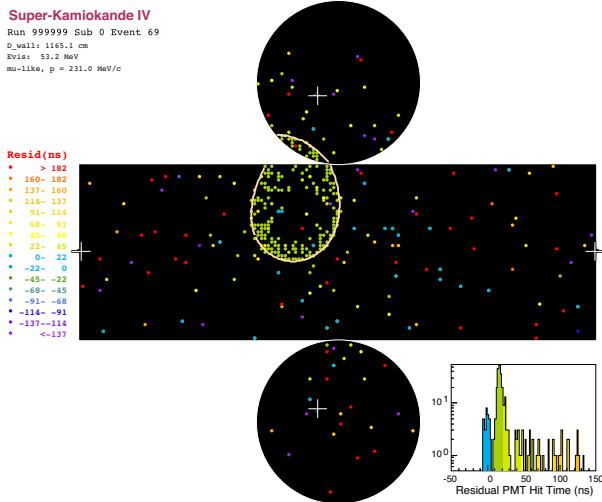
FIG. 3: (color online) An example graphical event display of a simulated proton decay passing all of the criteria for Method 1. The single Cherenkov ring was produced by the muon from kaon decay and fit with momentum 231 MeV/c. The color of the hit PMTs represents the residual hit time after subtracting the time-of-flight of Cherenkov light in water from the vertex to the PMT. The hit PMTs associated with a 6 MeV prompt gamma are colored cyan. The decay electron was detected after the displayed event.
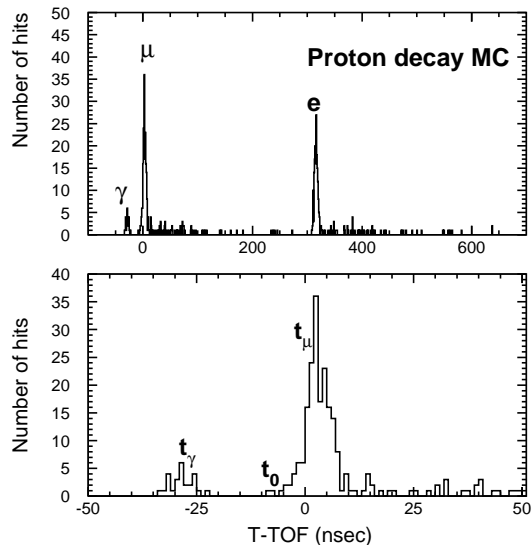

FIG. 4: Number of hits versus hit time for a typical proton decay MC event selected by Method 1. In the upper figure, three hit clusters due to prompt γ, μ, and the Michel electron can be seen in order. The lower figure is expanded around the μ-cluster and t_γ, t_0, and t_μ are shown as a demonstration.

The proton identification criterion (A-6) is a refinement to the methods in our previous paper for rejecting single proton ring events. It is used for reduction of single proton ring events. The algorithm [31] makes a likelihood function assuming a muon (L_μ) and a proton (L_{pr}) by using the Cherenkov angle and the width of the Cherenkov ring. Figure 5 shows the likelihood function. The upper figure is for the sample requiring cuts (A-1) through (A-5). Data and MC agree well. The lower figure is the same distribution after applying cuts (A-7) and (A-8) additionally. Background events are efficiently reduced by (A-6).
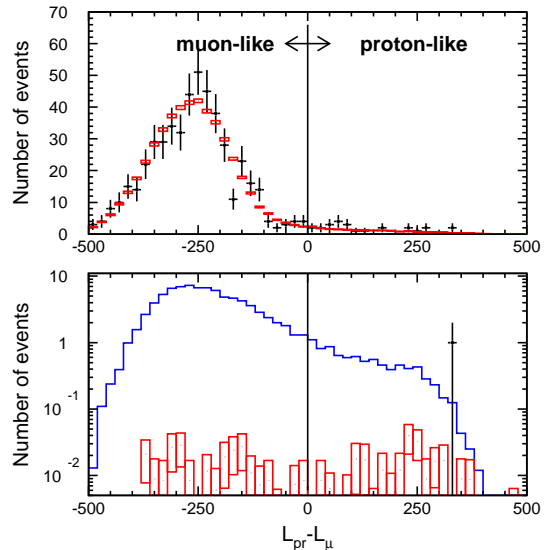

FIG. 5: (color online) The likelihood distribution to separate μ and proton. The negative region is μ-like and positive is proton-like. In the upper figure, the atmospheric ν MC (box) is compared with data merging SK-I/III/IV (dot) requiring cuts (A-1) through (A-5), and they are in good agreement. The lower figure shows the same distributions after γ-tagging cuts; the remaining background is reduced by the likelihood cut.

After cuts (A-1) through (A-6), a distribution of hits (N) vs. time after TOF subtraction (t) is made. To search for the prompt gamma ray, three quantities of time must be defined. The first is t_μ, which represents the time associated with the detection of the muon, or equivalently, the decay of the kaon. The second is t_0, which is the start time to search in the past time distribution of hits to find the prompt gamma ray hits. The third is t_γ, which is the associated time of the gamma ray detection. PMTs outside of a 50° cone with respect to the muon direction are masked and t_μ is defined as the time where dN/dt is maximum. The signal of the gamma ray is so tiny, compared to the muon, that it can easily be hidden by muon hits. To avoid this, the gamma finding is started earlier than the muon hits. To determine t_0, dN/dt is calculated from the muon peak time into the past. Muon hits are dominant while $dN/dt > 0$, and t_0 is defined at the point where dN/dt changes to less than or equal to 0. Then, in the N-versus-t distribution, a time window with 12 nsec width is slid backward

from t_0. The associated time of the gamma ray candidate, t_γ, is defined as the middle of the time window where the number of hits in the window is maximum, N_γ.

Figure 6 shows the N_γ distribution for SK-I, III, and IV in the upper figure and SK-II in the lower figure after all cuts except (A-7). An arrow in the figure shows the signal region, i.e. with cut (A-7) applied; there are no data in this region.
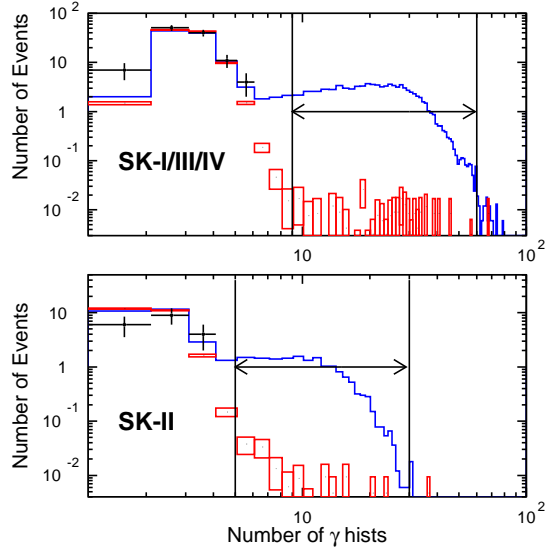

FIG. 6: (color online) Number of γ ray hit distributions. The upper figure shows sum of SK-I, III, and IV which have 40% photo coverage, the lower figure corresponds to SK-II with 19% photo coverage. Dots, squares, and histogram correspond to data, atmospheric ν MC normalized to livetime of data, and proton decay MC with arbitrary normalization, respectively. The signal regions are indicated by arrows. The peaks at small numbers of hits are due to dark hits of the PMTs.

Table III show background rate per Megaton·year and expected events estimated by atmospheric ν MC, observed events in data, and efficiencies evaluated by the proton decay MC for each reduction step. SK-I, III, and IV which have 40% photo-coverage are merged and results of SK-II with 19% photo-coverage are separately shown.

The selection efficiencies, expected number of background, and observed number of events are summarized in Table V. The efficiency in SK-IV is higher than the other periods because the tagging efficiency for Michel electrons has been improved thanks to the new electronics described in the detector section. The total expected background for 260 kton·year exposure is 0.4 events, and no events are observed. The dominant neutrino interaction in the background expectation comes from $\Delta S = 0$ kaon production (48%): $\nu p \to \nu K^+ \Lambda$, where the Λ decays to unobserved proton and π^-. If the neutrino interaction is accompanied by de-excitation gamma rays, the event has the same configuration as the proton decay signal. The second most prevalent background is ν_μ charged current quasi-elastic scattering accompanied by de-excitation gamma rays (25%).

The dominant systematic error for the selection of signal is uncertainty in the de-excitation gamma ray emission probabilities. They are estimated to be 15% for the 6.3 MeV gamma ray and 30% for the others [23], and they contribute 19% to the overall systematic uncertainty on the selection efficiency. The other systematic uncertainties come from event reconstruction: energy scale, particle ID, ring-counting, fiducial volume, water scattering and attenuation parameters, and they range in size from 1% to 3%. In total, 22% is the systematic error of the selection. The uncertainty in the background rate comes from atmospheric neutrino flux and the cross section of neutrino interactions. The uncertainty in the neutrino flux is conservatively estimated to be 20% [26]. By changing the cross section of charged current quasi-elastic scattering, neutral current elastic scattering, and single π production interaction by $\pm 30\%$, and the deep inelastic scattering by $\pm 50\%$, a 10% uncertainty in background rate is found. The total systematic error for the background in Method 1 is estimated to be 25%.

There were several improvements in our analysis since our last paper about $p \to \nu K^+$ was published in 2005 [10]. As described in the reconstruction section, the time window for hits used to calculate momentum is changed if a Michel electron is closer than 250 nsec from the parent particle. This is a new algorithm which prevents the overestimation of the momentum due to including PMT hits from the Michel electron. Previously, the vertices of those events tended to be misfit in the forward direction since the precise fitter used the expected charge for each PMT based on an overestimated momentum with larger Cherenkov angle. This resulted in more TOF to be subtracted for hits backward of the particle direction and, as a result, it sometimes made fake prompt γ signals in atmospheric ν interactions. The improvement of the momentum calculation algorithm reduced the atmospheric ν background by a factor of three and eliminated a candidate event in the SK-IV data that would have survived based on the uncorrected algorithm. As a result, the expected background for the gamma-tag method in SK-I is reduced from the value in the previous paper 0.7 events, to 0.2 events while maintaining signal efficiency. The new selection criterion (A-6) further rejects 60% of the atmospheric background (after all other cuts) while losing only 8% efficiency. As a result, the expected background for Method 1 is greatly reduced, finally to 0.08 events for the SK-I period.

B. Method 2: $K^+ \to \mu^+ \nu_\mu$, mono-energetic muon search

Since most of the K^+s stop in water, the monoenergetic μ^+s from kaon decays would lead to an excess peak in the muon momentum distribution of atmospheric neutrino background. To avoid using the same events as in Method 1, Method 2 requires all the criteria in Method 1 except: the requirements in momentum (A-3) are relaxed to allow a spectrum fit, and the gamma hits (A-7) must not be present. We search for an excess of muon events in the momentum distribution by fitting the data with the proton decay signal expectation over the atmospheric neutrino background events. The signal and back-

	SK-I/III/IV				SK-II			
Criterion	Bkg. Rate	Exp. Bkg.	Data	Signal Eff.	Bkg. Rate	Exp. Bkg	Data	Signal Eff.
A-1	35240.8	7432.3	7497	0.575	34910.6	1717.6	1712	0.566
A-2	24865.7	5244.2	5240	0.520	22239.7	1094.2	1051	0.473
A-3	2496.6	526.5	531	0.494	2161.0	106.3	91	0.440
A-4	2443.7	515.4	520	0.485	2067.8	101.7	87	0.420
A-5	2400.3	506.2	514	0.479	2030.0	99.9	82	0.414
A-6	2302.7	485.6	488	0.436	1931.5	95.0	78	0.368
A-7	1.34	0.28	0	0.084	5.84	0.29	0	0.063
A-8	1.11	0.24	0	0.084	2.75	0.14	0	0.062

TABLE III: Event rates per Megaton·year and expected numbers of event from atmospheric ν MC, observed numbers of event in data, and signal efficiencies estimated from proton decay MC, for each step. SK-I/III/IV with 40% photo-coverage and SK-II with 19% are shown separately.

ground normalizations are free parameters in the fit. Figure 7 shows the muon momentum distribution of data from SK-I to SK-IV compared with MC. No significant excess is observed in the signal region, defined by vertical lines.
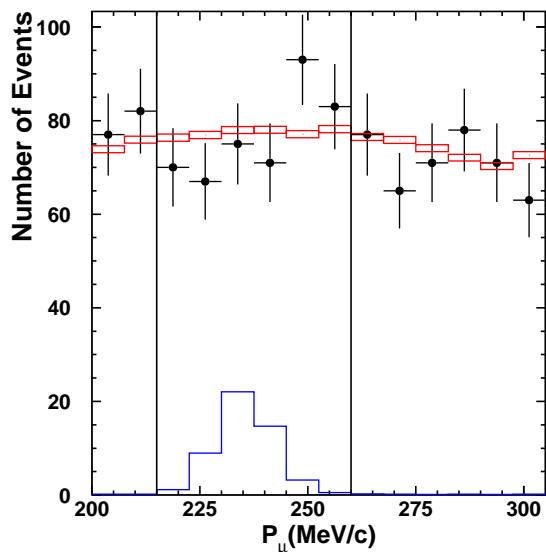

FIG. 7: (color online) Muon momentum distribution for 260 kton·year. Dots, boxes, and histogram correspond to data, atmospheric ν MC, and proton decay MC, respectively. The data are fit by the background plus signal by free normalization. No excess above the expected background is observed. The normalization of the proton decay MC histogram shown is at the upper limit allowed by the fit.

C. Method 3: $K^+ \rightarrow \pi^+ + \pi^0$

In Method 3, π^0 events with a momentum of 205 MeV/c are selected. An example event display is shown in Fig. 8.

The π^0 decays into two photons; if the energy of one photon is much smaller than the other, sometimes those events are misidentified as a single-ring event. A special π^0 reconstruction algorithm is used to search for proton decay candidates within the single-ring event sample. The π^+ does not make a clear Cherenkov ring due to its low momentum. However, hit activity in the opposite direction of the π^0, caused by the π^+, is used to identify the $K^+ \rightarrow \pi^+\pi^0$ signal. The following selection criteria are used:

(C-1) FC events with one or two rings and all rings are e-like,

(C-2) one Michel decay electron from the muon produced by π^+ decay,

(C-3) the reconstructed invariant mass of the π^0 candidate is between 85 and 185 MeV/c^2,

(C-4) the reconstructed momentum of the π^0 candidate is between 175 and 250 MeV/c,

(C-5) the residual visible energy associated with neither the π^0 nor the π^+ is low: $E_{res} < 12$ MeV for two-ring events and $E_{res} < 20$ MeV for single-ring events, E_{res} is described in latter,

(C-6) the likelihood for the photon distribution is consistent with that expected for signal events: $L_{shape} > 2.0$ for two-ring events and $L_{shape} > 3.0$ for single-ring events in SK-I/III/IV; $L_{shape} > 1.0$ for SK-II. L_{shape} is explained later.

(C-7) there is visible energy backwards from the π^0 direction consistent with a low momentum π^+: 10 MeV $< E_{bk} < 50$ MeV. A detailed description of E_{bk} is given later.

A special π^0 reconstruction algorithm is applied to the single-ring sample, which was developed for rejecting single-ring π^0 background from CC ν_e appearance in neutrino oscillations. The π^0 algorithm forces a fit to the best second ring by comparing the observed and the expected light patterns under the assumption of two electromagnetic showers and reconstructs the invariant mass and momentum of the π^0
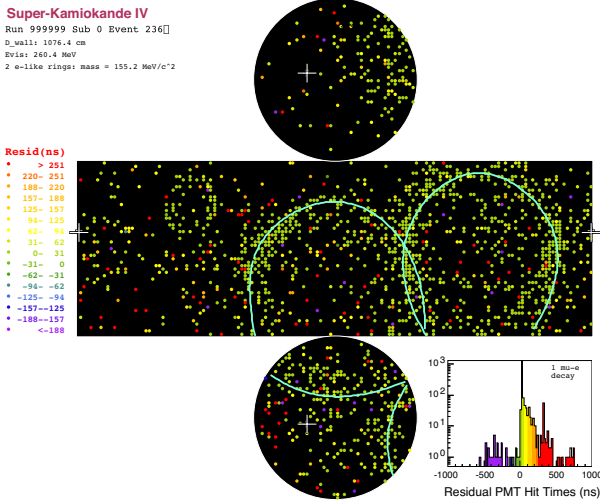
FIG. 8: (color online) An example graphical event display of a simulated proton decay passing all of the criteria for Method 3. The two Cherenkov rings were produced by gamma rays from π^0 decay and reconstructed to an invariant mass of 155 MeV/c^2 and momentum of 209 MeV/c. The color of the hit PMTs represents the residual hit time after subtracting the time-of-flight of Cherenkov light in water from the vertex to the PMT. The π^+ does not make a Cherenkov ring that is reconstructed, however PMT hits due to this particle are present opposite to the π^0 direction, visible in the upper left of the ID barrel region.
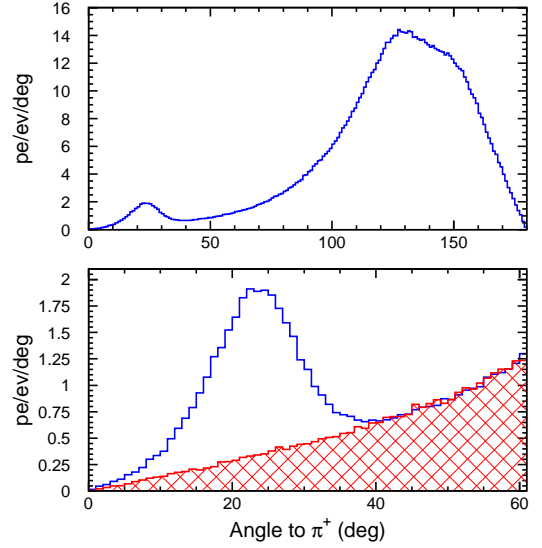

FIG. 9: (color online) Charge distribution as a function of angle to the π^+ direction which is defined as opposite the reconstructed π^0 direction. The upper figure shows the distribution for the signal MC in which K^+ decays into π^+ and π^0. The bump around 23° in the signal is made by Cherenkov light of π^+. The lower figure shows only the region from 0° to 60° for signal MC (blue) and atmospheric ν MC (hatched red) after the (C-1)-(C-5) criteria are required.
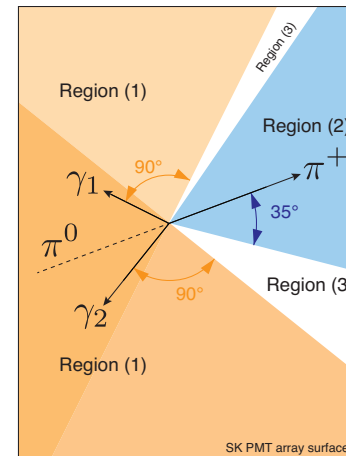
candidate. Then (C-3) and (C-4) can be applied even for the single-ring samples.

After selecting single π^0 candidates in the signal momentum region, and requiring a Michel electron, further cuts are applied to find the tiny Cherenkov light from the π^+. Figure 9 shows the photoelectron distribution versus angle for proton decay Monte Carlo events. The angle is calculated from the opposite direction of the reconstructed π^0, which can be assumed as the π^+ direction. The small bump around 23° comes from π^+.

The Cherenkov light in an event is then divided into three regions: (1) a π^0 dominant region, inside of 90° from each γ direction, (2) a π^+ dominant region, inside of 35° from the backwards direction from the reconstructed π^0 momentum vector, and (3) a residual region. These regions are illustrated in Fig. 10.

Visible energy sums are calculated for regions (2) and (3) by masking region (1) to define E_{bk} and E_{res} to be used in criteria (C-5) and (C-7), respectively. Non-zero E_{bk} is used to identify the presence of the π^+. By requiring low E_{res}, we reject background events with additional final state particles that produce Cherenkov light. In the case of a single-ring π^0 candidate, only the ring direction found by the default reconstruction is masked as region (1), because the other ring candidate found by the π^0 special algorithm is often found at a large angle from the existing ring direction due to asymmetric decay, and if the 90° cone of the additional ring is masked, the π^+ direction may be also masked. In this case, the missing γ may exist in region (2) or (3), so the cut value for E_{res}

FIG. 10: (color online) An illustration showing each region for $K^+ \rightarrow \pi^+\pi^0$. Region (1) is an area which is inside of 90° from each γ direction, region (2) is an area which is inside of 35° from backward of reconstructed π^0 direction, and region (3) is defined as residual part.

is looser than in the two-ring case. The shape of the angular distribution seen in Fig. 9 is also useful to separate signal and background. Based on Fig. 9, the expected photoelectrons are generated assuming signal and background, and a likelihood function (L_{shape}) is calculated for use in (C-6). Then π^+ can be tagged by using deposited energy (E_{bk}) and shape

of charge distribution (L_{shape}). The shape of the angular distribution is slightly different in the single-ring and two-ring cases, and also depends on photo-coverage, so the cut value is tuned separately for SK-II. Figure 11 shows E_{res}, L_{shape}, and E_{bk} distributions of the two-ring sample of SK-I+III+IV data and the atmospheric ν MC normalized by livetime, after cuts from (C-1) through (C-4), with good agreement between data and simulation. Figures 12 through 15 show E_{res}, L_{shape}, and E_{bk} distributions after all cuts except the cut for itself.
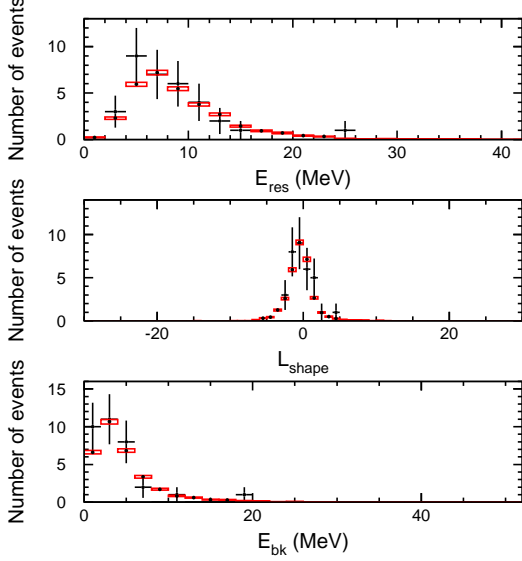

FIG. 11: (color online) E_{res} (upper), L_{shape} (middle), and E_{bk} (lower) distributions for the two-ring sample in SK-I,III, and IV after cuts from (C-1) through (C-4). Black crosses correspond to data and red histograms show the atmospheric ν MC normalized by livetime.

Table IV shows background rates per megaton·year exposure, expected events estimated by atmospheric ν MC, observed number of events in data, and efficiencies for each step. Results for SK-II, which has 19% photo-coverage are separately shown in the table. The selection efficiencies, expected numbers of background, and observed numbers of events for each period are summarized in Table V. The total expected background for 260 kton·year exposure is 0.6 events. No events are observed in the SK data. The dominant neutrino interaction modes in the background are charged current single π production (38%) with low momentum μ, kaon production (37%) described in Method 1, and neutral current multi-π production (11%).

The uncertainty for the π^0 fitter is rather large, 18% [32], but is only applied to the fraction of the single-ring π^0 sample (19%) with a final systematic error of 4.5%. The leading systematic uncertainty in the signal efficiency of Method 3 is in the π^+ interaction in water, estimated to be 5%. Including other reconstruction errors as listed for Method 1, the total systematic uncertainty in the signal efficiency of Method 3 is estimated to be 9.5%. The systematic uncertainty for the background in Method 3 is estimated to be 29% based on the
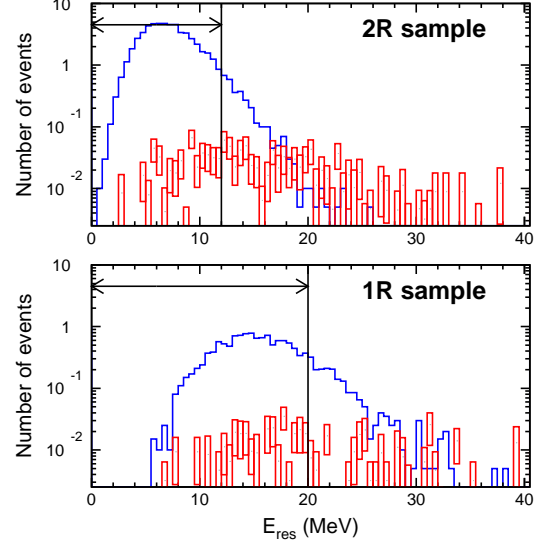

FIG. 12: (color online) E_{res} distributions for the two-ring (upper) and single-ring (lower) samples after all cuts except (C-5) in all periods. Red histograms are atmospheric ν MC, and blue histograms are proton decay MC, respectively. No data remain after cuts. Arrows in the figures show signal regions.
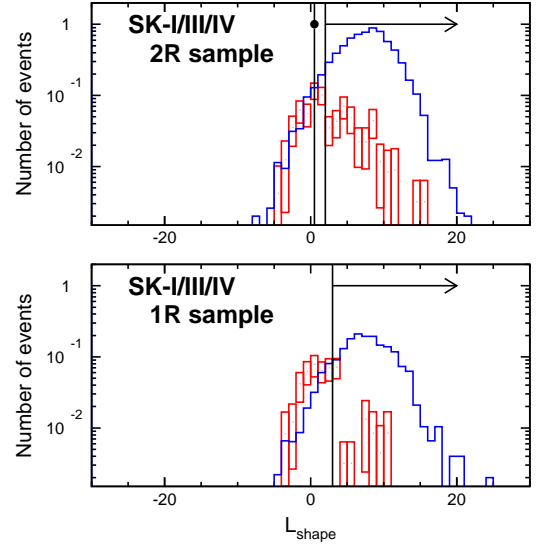

FIG. 13: (color online) L_{shape} distributions for the two-ring (upper) and single-ring (lower) samples for SK-I,III, and IV, after all cuts except (C-6). Black dots correspond to data, red histograms are atmospheric ν MC normalized to the livetime of data, and blue histograms are proton decay MC, respectively. Arrows in the figures show signal regions.

	SK-I/III/IV				SK-II			
Criterion	Bkg. Rate	Exp. Bkg.	Data	Signal Eff.	Bkg. Rate	Exp. Bkg	Data	Signal Eff.
C-1	51874.1	10940.3	10945	257	53574.1	2635.8	2615	0.277
C-2	5275.4	1112.6	1126	0.191	5421.1	266.7	300	0.191
C-3	1003.9	211.7	200	0.153	1266.7	62.3	56	0.137
C-4	225.6	47.6	42	0.131	244.1	12.0	10	0.114
C-5	171.8	36.2	37	0.120	178.1	8.76	7	0.101
C-6	10.1	2.13	2	0.098	15.9	0.780	0	0.775
C-7	2.09	0.44	0	0.087	3.42	0.17	0	0.067

TABLE IV: Event rates per Megaton·year and expected numbers of event from atmospheric ν MC, observed numbers of event in data, and signal efficiencies estimated from proton decay MC, for method 3. SK-I/III/IV with 40% photo-coverage and SK-II with 19% are shown separately.
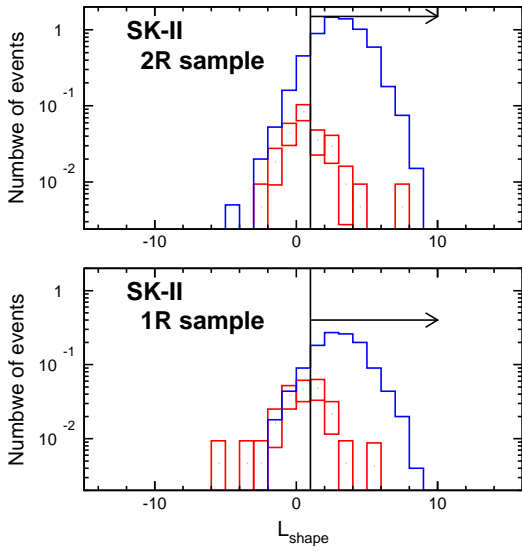

FIG. 14: (color online) L_{shape} distributions for the two-ring (upper) and single-ring (lower) samples for SK-II after all cuts except (C-6), respectively. Red histograms are atmospheric ν MC, and blue histograms are proton decay MC. No data remain after cuts. Arrows in the figures show signal regions.

FIG. 15: (color online) E_{bk} distributions for the two-ring (uper) and single-ring (lower) samples after all cuts except (C-7) in all periods. Black dots correspond to data, red histograms are atmospheric ν MC, and blue histograms are proton decay MC, respectively. Arrows in the figures show signal regions.

uncertainties in atmospheric neutrino flux and cross section following the same procedure as described for Method 1.

Compared to our previous publication, Method 3 is improved in efficiency by the addition of the single-ring π^0 sample which occupies 19% of the selected events in the signal MC. The angle cut at 40° applied to calculate the charge sum in region (2) in the previous paper was rather loose (refer to Figure 9). The cut value was tuned to 35° by maximizing $S/\sqrt{N}$ to reduce more background. The new variable L_{shape} also reduces background. As a result, the efficiency of Method 3 is increased by 30% and the background is reduced by 30% from the previously published result for SK-I. The efficiencies, backgrounds, and observed events are summarized in Ta-
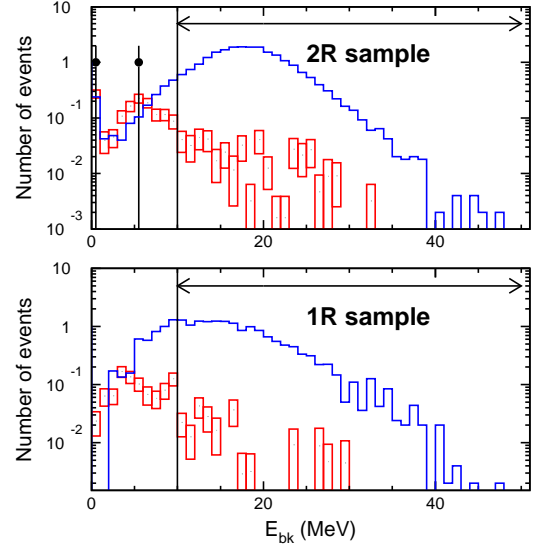
ble V. The efficiency in SK-IV is larger than the other periods because of the improvement in efficiency for Michel electron tagging.

D. Lifetime Limit

In the absence of any excess signal above the background expectation, we calculate the lower limit on the proton partial lifetime using a Bayesian method [33] to incorporate systematic uncertainty. The calculation method used in our previous publication [10] is applied in this analysis.

For Methods $i = 1$ and 3, where n_i is the number of can-

		SK-I	SK-II	SK-III	SK-IV
Exp.(kton·yrs)		91.7	49.2	31.9	87.3
Prompt γ	Eff.(%)	7.9±0.1	6.3±0.1	7.7±0.1	9.1±0.1
	BKG/Mt·yr	0.8±0.2	2.8±0.5	0.8±0.3	1.5±0.3
	BKG	0.08	0.14	0.03	0.13
	OBS	0	0	0	0
P_μ spec.	Eff.(%)	33.9±0.3	30.6±0.3	32.6±0.3	37.6±0.3
	BKG/Mt·yr	2107±39	1916±35	2163±40	2556±47
	BKG	193	94.3	69.0	223.1
	OBS	177	78	85	226
$\pi^+\pi^0$	Eff.(%)	7.8±0.1	6.7±0.1	7.9±0.1	10.0±0.1
	BKG/Mt·yr	2.0±0.4	3.4±0.6	2.3±0.4	2.0±0.3
	BKG	0.18	0.17	0.09	0.18
	OBS	0	0	0	0

TABLE V: Summary of the proton decay search with selection efficiencies and expected backgrounds for each detector period.

didate events in the i-th proton decay search, the conditional probability distribution for the decay rate is expressed as:

$$P(\Gamma|n_i) = \iiint \frac{e^{-(\Gamma\lambda_i\varepsilon_i+b_i)}(\Gamma\lambda_i\varepsilon_i+b_i)^{n_i}}{n_i!} \times$$
$$P(\Gamma)P(\lambda_i)P(\varepsilon_i)P(b_i)\,d\lambda_i\,d\varepsilon_i\,db_i \quad (1)$$

where λ_i is the true detector exposure, ε_i is the true detection efficiency including the meson branching ratio, and b_i is the true number of background events. The decay rate prior probability distribution $P(\Gamma)$ is 1 for $\Gamma \geq 0$ and otherwise 0.

The prior probability distributions incorporating uncertainties in detector exposure $P(\lambda_i)$, efficiency $P(\varepsilon_i)$, and background $P(b_i)$, are expressed as:

$$P(\lambda_i) = \delta(\lambda_i - \lambda_{0,i}) \quad (2)$$
$$P(\varepsilon_i) = \exp\left[-(\varepsilon_i - \varepsilon_{0,i})^2/2\sigma_{\varepsilon,i}^2\right] \quad (3)$$
$$(0 \leq \varepsilon_i \leq 1, \text{ otherwise } 0)$$
$$P(b_i) = \int_0^\infty \frac{e^{-b'}(b')^{b_{0,i}}}{b_{0,i}!}\exp\left[\frac{-(b_iC_i-b')^2}{2\sigma_{b,i}^2}\right]db' \quad (4)$$
$$(0 \leq b_i, \text{ otherwise } 0)$$

where $\lambda_{0,i}$ is the estimated exposure, $\varepsilon_{0,i}$ is the estimated efficiency, $b_{0,i}$ is the estimated number of background events in 500 years MC, C_i is the MC-to-exposure normalization factor, and $\sigma_{\varepsilon,i}$ and $\sigma_{b,i}$ are the uncertainties in detection efficiency and background, respectively.

To combine Method 2, the remaining events are divided into three momentum bins: 200-215 MeV/c, 215-260 MeV/c, and 260-305 MeV/c and the number of observed events are denoted as m_1, m_2, m_3 instead of n_i. Then, the nucleon decay rate probability, $P(\Gamma|m_1, m_2, m_3)$, is calculated as:

$$P(\Gamma|m_1,m_2,m_3) = \iiint \prod_{j=1}^{3} \frac{e^{-(\Gamma\lambda_j\varepsilon_j+b_{shape,j}b)}(\Gamma\lambda_j\varepsilon_j+b_{shape,j}b)^{m_j}}{m_j!}P(\Gamma)P(\lambda_j)P(\varepsilon_j)P(b)P(b_{shape,j})\,d\lambda_j\,d\varepsilon_j\,db\,db_{shape,j}, \quad (5)$$

where $j = 1, 2, 3$ corresponds to each momentum bin, $P(b)$ is defined as one for $b > 0$ and otherwise 0, and ε_j denotes the efficiency for each bin. The number of background events, $b_{shape,j}$, is b_j normalized by b_2. The uncertainty function of the background shape $P(b_{shape,j})$ is defined by a Gaussian function for the 1st and 3rd bin, and a delta function for the 2nd bin. The uncertainties of the background are estimated to be 7% and 8% respectively from the difference of MC models.

We combine all three searches to calculate the lower limit of the nucleon decay rate, Γ_{limit} as:

$$CL = \frac{\int_{\Gamma=0}^{\Gamma_{\text{limit}}}\prod_{i=1}^{N=3}P(\Gamma|n_i)\,d\Gamma}{\int_{\Gamma=0}^{\infty}\prod_{i=1}^{N=3}P(\Gamma|n_i)\,d\Gamma}, \quad (6)$$

where $N = 3$ is the number of independent search methods[2], and CL is the confidence level, taken to be 90%. The lower

lifetime limit is given by:

$$\tau/B_{p\to\nu K^+} = \frac{1}{\Gamma_{\text{limit}}}\sum_{i=1}^{N}[\varepsilon_{0,i}\cdot\lambda_{0,i}]. \quad (7)$$

The result of the limit calculation combining the three search methods is:

$$\tau/B_{p\to\nu K^+} > 5.9 \times 10^{33}\text{years},$$

at the 90% confidence level. If only the results of the low background searches are used, Methods 1 and 3, the lower limits of proton lifetime are estimated to be 2.5×10^{33} and 2.6×10^{33} years, respectively. The lifetime limit from the muon momentum spectrum fit, Method 2, is 0.8×10^{33} years.

VI. CONCLUSION

The proton decay search for $p \to \nu K^+$ was carried out with 260 kton·year exposure, including SK-I, II, III, and IV. There

---

[2] for $i = 2$, the second search method, $P(\Gamma|n_2) \equiv P(\Gamma|m_1, m_2, m_3)$

are several improvements in the analysis and we succeeded to reduce backgrounds drastically and to increase efficiencies. However, we do not find any evidence for proton decay in this exposure, therefore we have set a limit on the partial lifetime as 5.9×10^{33} years, which is more than 2.5 times more stringent than our previous publication. The non-observation of proton decay into this mode constrains, but does not exclude, recent SUSY GUT models.

VII. ACKNOWLEDGMENTS

[1] H. Georgi and S. L. Glashow, Phys. Rev. Lett. **32**, 438 (1974).
[2] C. McGrew *et al.*, Phys. Rev, D **59**, 052004 (1999).
[3] K. S. Hirata *et al.*, Phys. Lett, B **220**, 308 (1989).
[4] M. Shiozawa *et al.*, Phys. Rev. Lett. **81**, 3319 (1998); H. Nishino *et al.*, Phys. Rev. Lett. **102**, 141801 (2009).
[5] Y. Hayato *et al.* [Super-Kamiokande Collaboration], Phys. Rev. Lett. **83**, 1529 (1999) [hep-ex/9904020].
[6] J. Wess and B. Zumino, Nucl. Phys. B **70**, 39 (1974).
[7] W. J. Marciano and G. Senjanovic, Phys. Rev. D **25**, 3092 (1982).
[8] N. Sakai and T. Yanagida, Nucl. Phys. B **197**, 533 (1982); S. Weinberg, Phys. Rev. D **26**, 287 (1982).
[9] H. Murayama and A. Pierce, Phys. Rev. D **65**, 055009 (2002).
[10] K. Kobayashi *et al.*, Phys. Rev. D **72**, 052007 (2005).
[11] K. S. Babu, B. Bajc and Z. Tavartkiladze, Phys. Rev. D **86**, 075005 (2012); T. Goto and T. Nihei, Phys. Rev, D **59**, 115009 (1999).
[12] K. S. Babu, J. C. Pati and Z. Tavartkiladze, JHEP **1006**, 084 (2010); V. Lucas and S. Raby, Phys. Rev. D **55**, 6986 (1997).
[13] S. Fukuda *et al.*, Nucl. Inst. and Meth. A **501**, 418 (2003).
[14] H. Kume *et al.*, Nucl. Inst. and Meth. **205**, 443 (1983); A. Suzuki *et al.*, Nucl. Inst. and Meth. A **329**, 299 (1993).
[15] H. Nishino *et al.*, Nucl. Inst. and Meth. A **610**, 710 (2011); S. Yamada *et al.*, IEEE Trans. Nucl. Sci. 57, 2010, 428.
[16] K. Abe *et al.*, submitted to Nucl. Inst. and Meth. A [arXiv:1307.0162].

[17] K. Abe *et al.*, Phys. Rev. Lett. **110**, 181802 (2013); K. Abe *et al.*, Phys. Rev. Lett. **107**, 241801 (2011); R. Wendell *et al.*, Phys. Rev. D **81**, 092004 (2010) (and more relevant references).
[18] K. Nakamura *et al.*, Nucl. Phys. A **268**, 381 (1976).
[19] T. Yamazaki and Y. Akaishi, Phys. Lett. B **453**, 1 (1999).
[20] R. D. Woods and D. S. Saxon, Phys. Rev. **95**, 577 (1954).
[21] Y. Hayato, Nucl. Phys. Proc. Suppl. **112**, 171 (2002); G. Mitsuka, AIP Conf. Proc. **967**, 208 (2007); G. Mitsuka, AIP Conf. Proc. **981**, 262 (2008).
[22] D. Rein and L.M. Sehgal, Ann. of Phys. **133**, 1780 (1981).
[23] H. Ejiri, Phys. Rev. C **48**, 1442 (1993).
[24] H. Nishino *et al.*, Phys. Rev. D **85**, 112001 (2012).
[25] C. Regis *et al.*, Phys. Rev. D **86**, 012006 (2012).
[26] M. Honda, T. Kajita, K. Kasahara, S. Midorikawa, and T. Sanuki, Phys. Rev. D **75**, 043006 (2007).
[27] CERN Program Library W5013 (1994).
[28] M. Nakahata *et al.*, J. Phys. Soc. Jpn. **55**, 3786 (1986); A. S. Clough *et al.*, Nucl. Phys. B **76**, 15 (1974).
[29] J. P. Albanese *et al.*, Nucl. Phys. A **350**, 301 (1980); C. H. Q. Ingram *et al.*, Phys. Rev. C **27**, 1578 (1983).
[30] E. R. Davies, *Mahine Vision: Theory, Algorithms, Practicalities*, Academic Press, Sandiego (1997).
[31] M. Fechner *et al.*, Phys. Rev. D **79**, 112010 (2009).
[32] T2K collaboration., Phys. Rev. Lett. **107**, 041801 (2011).
[33] C. Amsler *et al.*, Phys. Lett. B **667**, 1 (2008).